

Early science with the Large Millimetre Telescope: Fragmentation of molecular clumps in the Galaxy

M. Heyer^{1*}, G. W. Wilson¹, R. Gutermuth¹, S. Lizano², A. Gomez-Ruiz³,
S. Kurtz², A. Luna³, E. O. Serrano Bernal³, and Schloerb, F.P.¹

¹*Department of Astronomy, University of Massachusetts, Amherst, MA 01003, USA*

²*Instituto de Radioastronomía y Astrofísica, Universidad Nacional Autónoma de México, 58089 Morelia, Michoacán, México*

³*CONACYT-Institut Nacional de Astrofísica, Óptica y Electrónica, Luis E. Erro 1, 72840 Tonanzintla, Puebla, México*

Accepted XXX. Received YYY; in original form ZZZ

ABSTRACT

Sensitive, imaging observations of the $\lambda 1.1$ mm dust continuum emission from a 1 deg^2 area collected with the AzTEC bolometer camera on the Large Millimeter Telescope are presented. A catalog of 1545 compact sources is constructed based on a Wiener-optimization filter. These sources are linked to larger clump structures identified in the Bolocam Galactic Plane Survey. Hydrogen column densities are calculated for all sources and mass and mean volume densities are derived for the subset of sources for which kinematic distances can be assigned. The AzTEC sources are localized, high density peaks within the massive clumps of molecular clouds and comprise 5-15% of the clump mass. We examine the role of the gravitational instability in generating these fragments by comparing the mass of embedded AzTEC sources to the Jeans' mass of the parent BGPS object. For sources with distances less than 6 kpc the fragment masses are comparable to the clump Jeans' mass, despite having isothermal Mach numbers between 1.6 and 7.2. AzTEC sources linked to ultra-compact HII regions have mass surface densities greater than the critical value implied by the mass-size relationship of infrared dark clouds with high mass star formation while AzTEC sources associated with Class II methanol masers have mass surface densities greater than 0.7 g cm^{-2} that approaches the proposed threshold required to form massive stars.

Key words: ISM:clouds – ISM:molecules – ISM: structure – stars:formation – sub-millimetre:ISM

1 INTRODUCTION

The density structure of a molecular cloud is a roadmap for recent and impending sites of star formation within its domain. New stars develop within gravitationally unstable protostellar cores in which most of the available gas is subsumed into the star or circumstellar disk (Krumholz & Tan 2007; André et al. 2014). The protostellar cores reside within larger structures such as clumps and filaments that have mean densities of 10^{3-5} cm^{-3} , sizes between 0.5 and several pc, and masses ranging from 100 to $10^4 M_{\odot}$ (André et al. 2014; Svoboda et al. 2016). These features are embedded within larger molecular clouds that span 10-50 pc in size, have mean volume densities of 10^{2-3} cm^{-3} , and masses ranging from 10^4 to $10^6 M_{\odot}$ (Heyer & Dame 2015). Understanding the processes responsible for cloud fragmentation from

clouds to clumps to protostellar cores is essential to developing improved descriptions of star formation in galaxies. An important issue to address is the efficiency with which mass is redistributed into ever more dense gas configurations in each stage of fragmentation. This efficiency can regulate the star formation rate in molecular clouds and may also impact the distribution of stellar masses of the newborn stars.

Recent imaging surveys of the dust continuum emission along the Galactic plane illustrate the complex structure of the dense molecular interstellar medium and provide a broad census of protostellar cores and clumps throughout the Milky Way. The Apex Telescope Large Area Survey of the Galaxy (ATLASGAL) surveyed the $870\mu\text{m}$ dust emission between longitudes -60 to 60 degrees (Schuller et al. 2009). The Bolocam Galactic Plane Survey (BGPS) imaged the 1.1 mm dust emission from the Central Molecular Zone (CMZ), the first quadrant of the Galaxy, and targeted star forming regions in the Outer Galaxy (Ginsburg et al. 2013).

* Email: heyer@astro.umass.edu

The Herschel Infrared Galactic Plane Survey (HI-GAL) imaged the dust emission in five far infrared wavelength bands between 70 and 500 μm (Molinari et al. 2016). These programs have identified thousands of compact sources that include dense prestellar and protostellar cores and massive clumps at angular resolutions between 19'' and 35''. To examine the structure within a dust source that represents the next stage of fragmentation, one requires higher angular resolutions typically afforded by mm-wave interferometers. However, owing to the small field-of-view of interferometers, the number of targets one can investigate is rather limited and subject to selection bias.

With the operation of the Large Millimeter Telescope (LMT) in Mexico that is equipped with the AzTEC bolometer array at λ 1.1 mm, one can collect high sensitivity imaging observations of the dust continuum emission over large areas of the sky at 8.5'' angular resolution. Such imaging offers an unbiased census of cold, compact cores that may constitute the next level of cloud fragmentation in the interstellar medium (ISM). Here, we report on results from imaging of the λ 1.1 mm dust continuum emission over a 1 deg² field centered at the Galactic longitude of 24°.5 with the LMT. This line of sight through the Galaxy crosses the stellar bar, the near and far sides of both the Sagittarius and Scutum spiral arms and the far side Perseus and Norma-Cygnus arms. Therefore, the field covers a broad range of Galactic radii and interstellar conditions. The LMT data are complemented with measurements from the recent Galactic plane surveys of the dust and radio continuum emissions, and molecular line emission.

2 DATA

The 32 meter Large Millimeter Telescope Alfonso Serrano was used with the AzTEC camera (Wilson et al. 2008) to image the λ 1.1 mm dust continuum emission from \sim 1 deg² area centered on the Galactic coordinates (24.5, 0). The half-power beam width at this wavelength is 8.5''. The observations were carried out in Spring 2016 as part of the Early Science-4 cycle of the LMT. Data were collected using On-the-Fly (OTF) mapping in which the telescope is rapidly scanned in azimuth while continuously collecting data. Thirteen individual maps were collected over several nights of observations. The mean atmospheric opacity was 0.23. The AzTEC calibration procedure is described in Wilson et al. (2008). Accounting for optical loading, bolometer responsivities, extinction corrections, and flux conversion factors for each bolometer, the fractional calibration error over a single night of observing is approximately 10% and decreases in quadrature over multiple nights of data collection. Pointing measurements on bright, nearby point sources are made approximately every hour throughout the night. Positional errors relative to a recent pointing measurement are typically 1''.

The data were processed with the AzTEC pipeline to remove atmospheric contributions, to account for pointing corrections, to calibrate the data, and to coadd the ensemble of maps (Scott et al. 2008). A noise map is constructed from jack-knifed noise realizations of each AzTEC map in which the time stream is randomly multiplied by ± 1 . The effect of the jack-knife step is to remove sources while retaining noise

properties. Each jack-knifed time-stream is converted into a map and coadded in weighted quadrature to produce a final image of rms noise values, σ . The final images of surface brightness and weights ($1/\sigma^2$) are constructed in equatorial coordinates (J2000). To compare with other data sets, the images are rotated into Galactic coordinates with the angle $-62^\circ.6$ that is appropriate for this segment of the Galactic plane.

3 RESULTS

The primary data products from the AzTEC pipeline are an image of λ 1.1 mm surface brightness and a corresponding noise image that reflects both instrumental and atmospheric contributions to the noise budget. Figure 1 shows the image of surface brightness rotated to the Galactic coordinate system. As with all OTF maps, the outer edges of the field have larger errors owing to fewer number of collected samples at these positions, and therefore, less accumulated time, relative to the central regions. Excluding these outer edges, the median surface brightness rms uncertainty is 9 mJy/beam with little variation within the boundary that encloses 70% of the data (solid line in Figure 1). This boundary approximates a circle with radius of 0.55 degree centered on $l, b = 24.5, 0$. We restrict our analysis to the area within this circle.

Within the processed image, any smoothly distributed emission component over angular scales greater than \sim 50'' is removed along with contributions from the atmosphere. This angular-dependent filtering is common to all ground-based millimeter and submillimeter camera systems with the filtering scale comparable to approximately half of the angular size of the field-of-view of the camera (Ginsburg et al. 2013). The effect of removing the extended emission component is that the residual signal is distributed into compact structures that are sites of higher column density and/or dust temperature with respect to the extended, interstellar cloud. These residual features generally correspond to the dense clumps and compact cores of molecular clouds.

The surface brightness image in Figure 1 shows several distinct clusters of compact emission features distributed throughout the field. Several of these clusters are associated with compact HII regions identified in radio continuum surveys (see §3.5). Members of an apparent cluster of AzTEC sources may be physically associated, residing in the same molecular cloud complex. However, additional velocity information for each member is required to more firmly establish this link. We note that different clusters and clouds in the field are located at varying distances and Galactic radii.

The image of observed surface brightness over the field does not effectively convey the measured structure within the image. The field is effectively 0.95 deg² in area while the detected signal is distributed into compact objects with angular sizes less than 50''. Figure 2 shows two subfields that illustrate the distribution of dust continuum emission detected by AzTEC over smaller angular scales following the application of the Wiener filter. The left image shows multiple, compact AzTEC sources (grey contours) within the domain of the BGPS emission at 34'' resolution, indicating fragmentation of this larger segment of a cloud. It also demonstrates the ability of the improved angular resolution

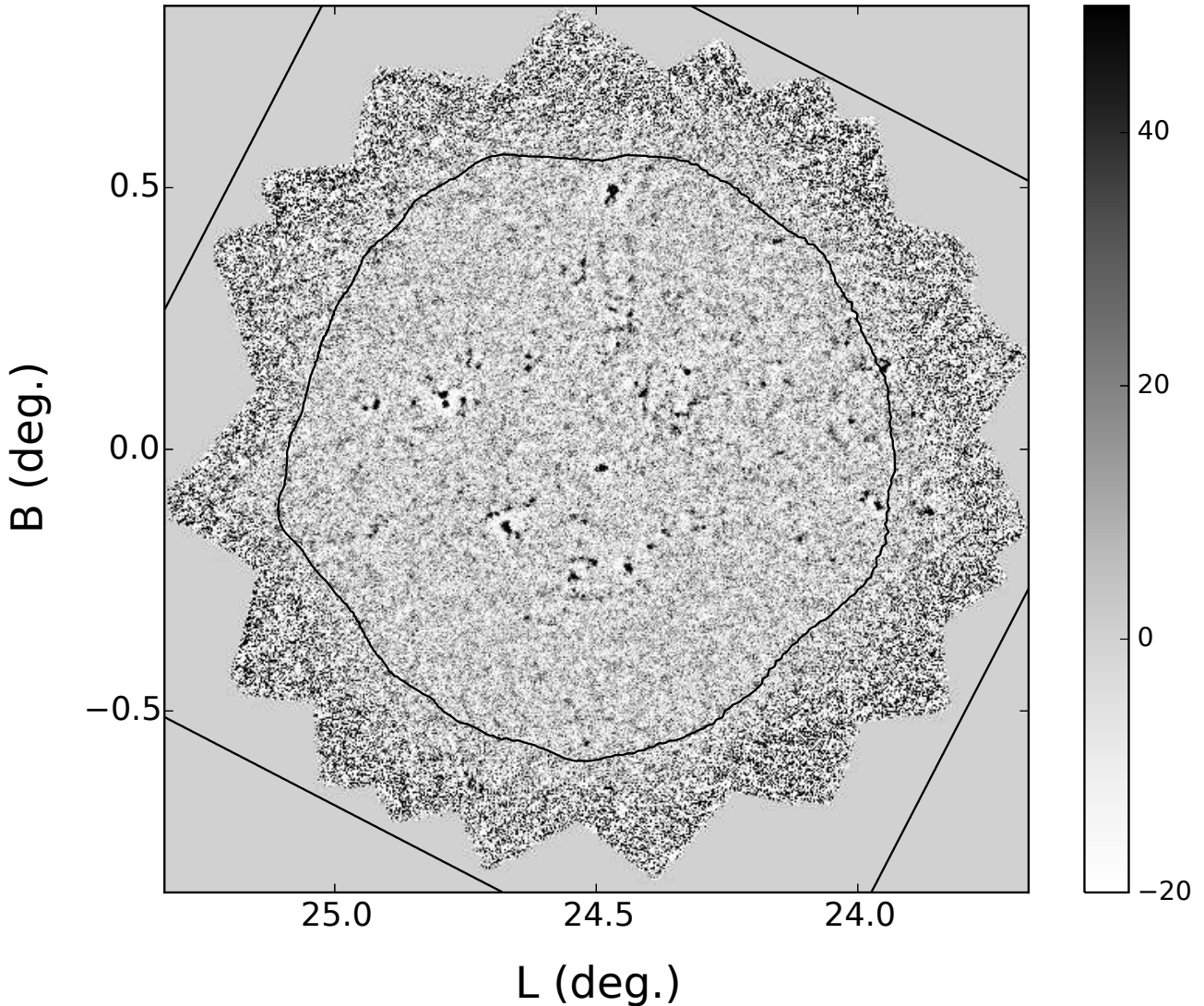


Figure 1. Image of $\lambda 1.1$ mm surface brightness over the observed field in units of mJy/beam. The contour marks the loci at which the rms image encloses 70% of the pixels.

of AzTEC on the LMT to more precisely locate the parcel of gas linked to the embedded ultra-compact HII (UCHII) regions that are highlighted in white contours. The right image shows a singular, bright AzTEC source embedded within a marginally resolved BGPS source. In this case, no fragmentation is evident at the $8.5''$ resolution of the AzTEC data. The peak dust emission is coincident with the Class II methanol maser G24.329+0.144 (Breen et al. 2015) that marks a very early phase of a developing massive star (Menten 1991).

3.1 Source Extraction

The improved sensitivity and angular resolution of the AzTEC data with respect to previous surveys of millimeter dust continuum along the Galactic plane motivates the

construction of a compact source list. To identify compact objects within the data, we apply the source extraction algorithm described by Perera et al. (2013), which is optimized for unresolved or marginally resolved features within the map. In brief, the functional form of the point spread function (PSF) is fit to each pixel in the image, which acts as an effective noise-reduction Wiener filter. Localized peaks in the resultant signal-to-noise image correspond to candidate point sources. In practice, the source may be unresolved along one direction but marginally extended along the orthogonal axis.

The source identification algorithm identifies 1545 source-candidates in the observed field with signal to noise greater than 3. Source positions in equatorial and Galactic coordinates, peak fluxes, uncertainties, and signal to noise (s2n) are derived from the fit of the PSF to the brightness

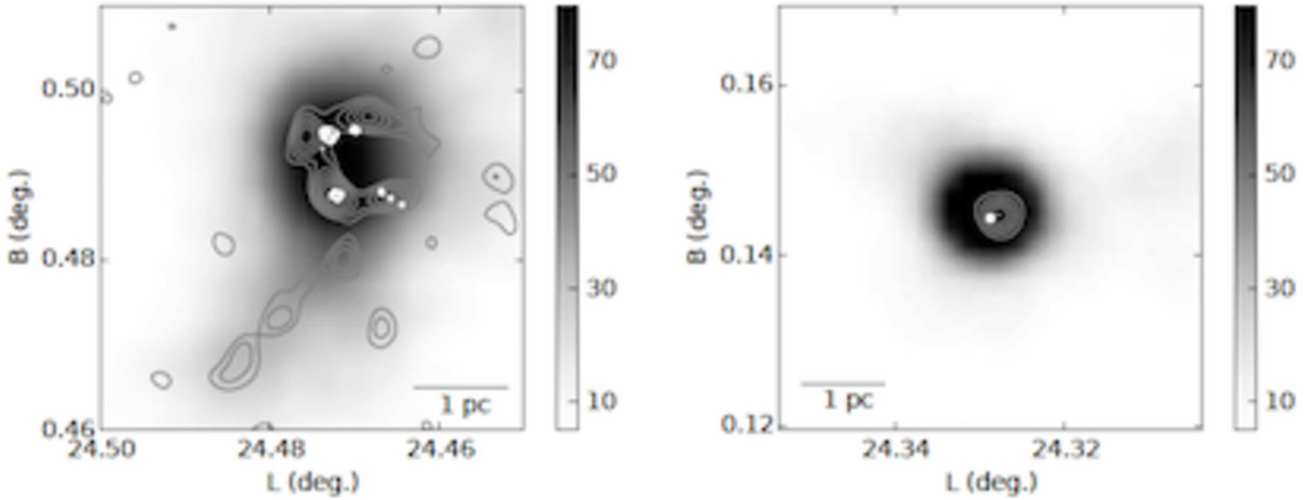


Figure 2. (left) The $\lambda 1.1$ mm dust continuum emission observed by the BGPS (halftone image) and AzTEC (grey contours) from the environment of a cluster of ultra-compact HII regions. Units are in MJy/steradian. The AzTEC contour levels range from 10-70 MJy/steradian spaced by 10 MJy/steradian. The white contours are 5 GHz radio continuum emission from CORNISH (Purcell et al. 2013). (right) BGPS and AzTEC images of $\lambda 1.1$ mm continuum emission from the environment of the Class II methanol maser, G24.329+0.144 (Breen et al. 2015). The solid white circle marks the location of the maser. The AzTEC contour levels range from 50 to 550 MJy/steradian spaced by 100 MJy/steradian.

distribution for all identified sources and are listed in Table 1. The median of the distribution of derived errors for the peak flux values is 7 mJy.

As part of the source identification process, 20 separate noise realizations of the data are searched for sources with the same algorithm to provide a measure of the expected number of false detections as a function of signal to noise. This analysis suggests that 30-50% of the sources with $s2n < 3.75$ within the field are false detections. This fraction attenuates with increasing signal to noise until limited by Poisson statistical errors. To quantify the probability of a false detection, we fit the expected fraction to an exponential decay curve for bins with $s2n < 5.25$ that are not limited by Poisson noise,

$$P_F(s2n) = P_F(3)\exp(-\alpha(s2n - 3.0)). \quad (1)$$

The best fit values are $P_F(3)=0.47$ and $\alpha=0.61$. Equation 1 describes a statistical expectation of the fraction of sources in each bin that are false. It does not identify or select which sources are false. One could simply exclude low signal to noise sources from further analysis but this selection criterion would also remove a significant number of valid sources.

To refine our measure of spurious sources, we construct a secondary probability function based on the angular distribution of $\lambda 1.1$ mm surface brightness independently measured by the BGPS that is more effective at recovering extended dust emission from clumps and clouds. Compact dust sources associated with potential or active sites of star formation are expected to reside within the boundaries of molecular clouds and clumps while false sources and contaminants such as background galaxies should be randomly distributed within the field. The probability that a randomly selected position in the field is coincident with a BGPS pixel ($7.2''$ in size) with surface brightness greater than I is equal

to the area subtended by these pixels normalized by the total area or equivalently,

$$P(I_{BGPS} > I) = \psi(I_{BGPS} > I) / \psi_T \quad (2)$$

where $\psi(I_{BGPS})$ is the number of BGPS pixels with surface brightness, I_{BGPS} , and ψ_T is the total number of BGPS pixels in the selected area. To evaluate equation 2, only BGPS pixels within the 0.55 degree radius are included.

From these two independent probability functions (equations 1 and 2) that a source is falsely identified as a compact, Galactic dust source, we calculate the joint probability distribution,

$$P_J = P_F(s2n)P(I_{BGPS} > I). \quad (3)$$

Figure 3 (left) shows the variation of $\log(P_J)$ in the $s2n$ - I plane. The drawn dotted contours represent P_J values 0.01, 0.05, 0.1, 0.2 from top to bottom. The horizontal solid line denotes the 1σ rms of 60 mJy/beam for the BGPS surface brightness in this field (Ginsburg et al. 2013).

For each AzTEC source, we evaluate P_J that effectively measures the probability that the source is false given its signal to noise ratio and location in the map with respect to the BGPS surface brightness distribution. These P_J values are listed in Table 1 for each source and can be used to select sources with increasing reliability (lower P_J). Figure 3 (right) shows the distribution of $\log(P_J)$ values for all AzTEC sources (light grey histogram) and for sources with $s2n < 3.5$ (dark grey histogram) that comprise most of the expected false detections.

Decreasing values of P_J reflect higher confidence that a given source is not false. For this study, we choose a limiting P_J value of 0.2. The number of sources excluded by this P_J value approximates the number of expected sources to be false for a given $s2n$ value but also considers the added infor-

Table 1. Identified AzTEC Sources. The full table is available in the electronic version of the paper.

AzTEC ID	Name	l (deg.)	b (deg.)	RA (deg.)	Dec (deg.)	$S_{1,1}$ (Jy)	$\sigma(S_{1,1})$ (Jy)	$\log(P_J)$
1	LMT_024.302+000.537	24.3024	0.5367	278.4203	-7.4269	0.031	0.010	-0.62
2	LMT_024.268+000.515	24.2682	0.5146	278.4242	-7.4674	0.030	0.010	-0.97
3	LMT_024.358+000.557	24.3581	0.5573	278.4277	-7.3680	0.028	0.009	-0.33
4	LMT_024.379+000.560	24.3791	0.5601	278.4350	-7.3480	0.029	0.009	-0.38
5	LMT_024.344+000.539	24.3444	0.5390	278.4378	-7.3886	0.031	0.009	-1.46
6	LMT_024.238+000.483	24.2376	0.4831	278.4382	-7.5091	0.033	0.009	-0.62
7	LMT_024.388+000.557	24.3884	0.5568	278.4423	-7.3413	0.029	0.009	-1.28
8	LMT_024.204+000.459	24.2042	0.4595	278.4437	-7.5497	0.033	0.009	-0.73
9	LMT_024.247+000.481	24.2473	0.4812	278.4443	-7.5013	0.032	0.009	-0.51
10	LMT_024.313+000.514	24.3130	0.5140	278.4456	-7.4280	0.028	0.009	-0.86

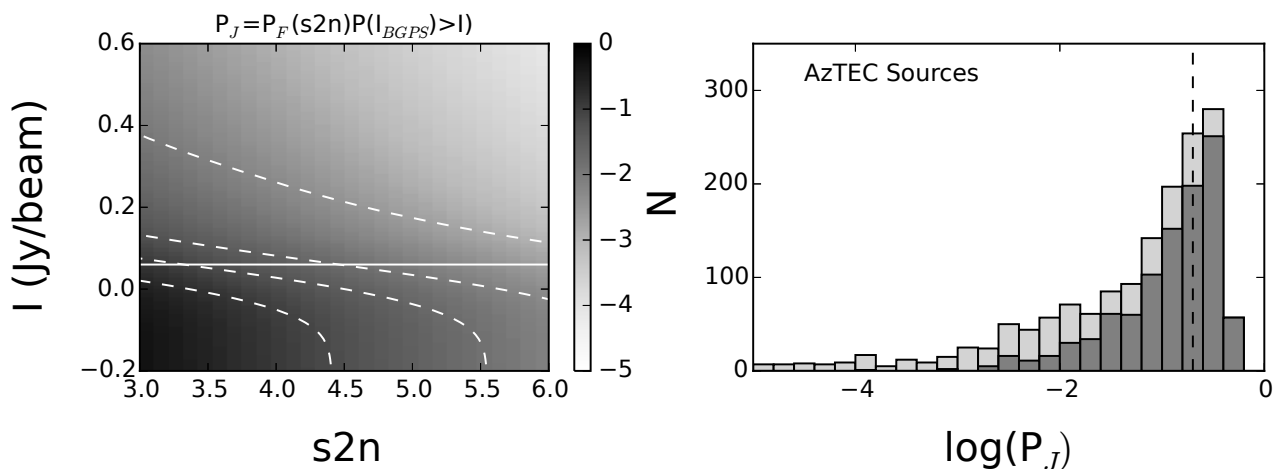


Figure 3. (left) The logarithm of the joint probability, P_J , of finding a false source with a given signal to noise to be coincident with a BGPS pixel with surface brightness greater than I within the observed field. The dotted contours show P_J values of 0.01, 0.05, 0.1, and 0.2 from top to bottom. The solid line is the median rms noise level of the BGPS for this field (Ginsburg et al. 2013). (right) Distribution of $\log(P_J)$ for all identified AzTEC sources (light-grey) and for sources with $s2n < 3.5$ (dark-grey). The vertical dotted line marks the joint probability threshold adopted by this study to select reliable sources, $P_J < 0.2$.

mation provided by BGPS imaging. There are 1095 sources with $P_J < 0.2$. This selection does not eliminate all low signal to noise sources but only those that fall into regions of low surface brightness as measured by the BGPS. Conversely, high signal to noise sources ($s2n > 4.5$) that are coincident with low BGPS surface brightness signal are considered valid and likely reflect the increased source sensitivity of the LMT data relative to the BGPS. This selection of sources can lead to a bias in which sources are spatially clustered but such a state is physically expected given the limited solid angle of molecular clouds and dense clumps in the ISM.

3.2 Linking AzTEC Sources to BGPS Sources

It is useful to compare sources identified by these AzTEC measurements with those of previous dust continuum imaging surveys of the Galactic plane measured with lower angular resolution. The BGPS is especially convenient as its detector bandpass is identical to that of AzTEC so no assumptions of the dust emissivity are required to make quantitative comparisons. Moreover, there is a large

amount of auxiliary information related to the BGPS sources including spectroscopy of high density gas tracers (Dunham et al. 2011; Schlingman et al. 2011; Shirley et al. 2013; Svoboda et al. 2016) and kinematic distance assignments (Ellsworth-Bowers et al. 2015a; Svoboda et al. 2016). This added information can be applied to the set of AzTEC sources that are linked to a given BGPS source.

To make this link, we use the image mask product provided by the BGPS Version 2.1 that marks the observed pixels for each BGPS source (Ginsburg et al. 2013). An AzTEC source is directly linked if its position falls within the solid angle of a BGPS source defined by the image mask. Table 2 lists the BGPS version 2 catalog number for each directly linked AzTEC source. We acknowledge that this method is not infallible. A fraction of the linked AzTEC sources could be foreground or background to the BGPS source. Ideally, one would require a spectroscopic velocity measurement of a dense gas tracer for each AzTEC source to directly relate it to the velocity-tagged BGPS source.

A comparison of the distribution of AzTEC sources with the BGPS objects shows several cases. First, there are 619

Table 2. AzTEC Sources Linked to BGPS Objects. Values of -999.0 indicate no velocity or distance measure is available. Column 7: the kinematic distance ambiguity resolution (kdar) flag – N (near), F (far), U (unknown). Column 8: source of dense gas velocity and distance measure– 0 (unknown) 1 (Ellsworth-Bowers et al. 2015a), 2 (Svoboda et al. 2016), 3 proximity to BGPS source with known distance, 4 (Roman-Duval et al. 2010), 5 (other). The full table is available in the electronic version of the paper

AzTEC ID	BGPS CNUM	V_{LSR} (km s^{-1})	D (kpc)	$-\sigma(D)$ (kpc)	$+\sigma(D)$ (kpc)	kdar	Ref
22	4058	93.6	10.1	0.2	0.2	F	2
26	4058	93.6	10.1	0.2	0.2	F	2
27	4067	96.3	5.1	0.3	0.3	N	1
29	4058	93.6	10.1	0.2	0.2	F	2
31	4040	-999.0	-999.0	-999.0	-999.0	U	0
33	4040	-999.0	-999.0	-999.0	-999.0	U	0
34	4067	96.3	5.1	0.3	0.3	N	1
39	4151	102.2	5.2	0.2	0.2	N	2
42	4116	102.0	5.3	0.2	0.2	N	2
44	4151	102.2	5.2	0.2	0.2	N	2

AzTEC sources with $P_J < 0.2$ that are linked to BGPS objects. Of the 255 BGPS catalogued objects within 0.55 degrees of the map center, there are 65 BGPS targets with a single AzTEC source and 124 BGPS targets with two or more AzTEC sources. This multiplicity within BGPS defined clumps is discussed further in §4. Second, there are 66 BGPS clumps with no AzTEC counterparts with $P_J < 0.2$. Given the improved sensitivity of the AzTEC data, the absence of any AzTEC sources would seem peculiar. We have visually inspected the BGPS images of these sources. In a few cases, the BGPS sources may be false positive detections. More typically, one finds low surface brightness emission with no significant substructure on scales less than the angular extent of the AzTEC footprint of ~ 50 - $100''$. In this case, the AzTEC processing to remove atmospheric contributions also subtracts any smooth, extended, diffuse component – leaving little or no residual signal to be identified by the AzTEC source extraction algorithm. Third, there are 476 AzTEC sources with $P_J < 0.2$ that have no BGPS counterpart. This can be attributed to the improved point source sensitivity and angular resolution of the AzTEC data.

3.3 Distribution in the Galaxy

With the linking of a subset of AzTEC sources to a given BGPS source, we poll the BGPS auxiliary data compiled by Ellsworth-Bowers et al. (2015a) and Svoboda et al. (2016) to assign velocities derived from a dense gas tracer (HCO^+ J=3-2 and NH_3 (1,1) inversion transition) and, if available, distances. Ellsworth-Bowers et al. (2015a) compute a Bayesian distance probability function to resolve the near-far side distance ambiguity using a set of priors for a large number of BGPS sources. Svoboda et al. (2016) extended the method using NH_3 observations. If available, we adopt these measures of distance to a linked AzTEC source. BGPS sources are frequently clustered spatially and kinematically. If a nearby BGPS object with an assigned distance is within $102''$ (3 BGPS half-power beam widths) of an AzTEC-linked BGPS object and its dense gas velocity is within 3 km s^{-1} of the linked BGPS object, then this distance is applied to all of the embedded AzTEC sources. Velocities and distances from these auxiliary data sets are listed in Table 2.

Not all BGPS objects linked to one or more AzTEC

sources have an established dense gas velocity or distance. In these cases, the ^{13}CO J=1-0 spectrum from the Boston University-FCRAO Galactic Ring Survey (GRS) (Jackson et al. 2006) at the AzTEC source position is examined. Such spectra frequently exhibit multiple velocity components as these lines of sight traverse several spiral arm features. A secondary velocity is assigned to the V_{LSR} value at which the antenna temperature of the coincident ^{13}CO J=1-0 spectrum is maximum. This peak temperature likely reflects enhanced column density or optically thick emission at this velocity within the $48''$ beam. In addition, we calculate a contrast value, C_v , defined as the ratio of the antenna temperatures at the velocity of the brightest ^{13}CO component to that of the next brightest component that is displaced by at least 5 km s^{-1} . C_v measures the degree to which the selected velocity component is distinguished from other components in the spectrum. The larger the contrast, the more likely this velocity is properly assigned to the AzTEC source. This velocity assignment from a ^{13}CO spectrum is not as conclusive as a spectrum from a dense gas tracer but is available for all 1545 AzTEC sources. For the 554 AzTEC sources with both a dense gas and ^{13}CO velocity, 493 (89%) have velocity differences, $|V_{\text{LSR}} - V(^{13}\text{CO})|$ less than 5 km s^{-1} . Restricting the sample to sources with $C_v > 1.5$ (452 sources), this fraction increases to 95%. The ^{13}CO -derived velocities and contrast values are compiled in Table 3.

If there is no BGPS-based distance information from a dense gas tracer, as in the case where the kinematic distance ambiguity could not be resolved, we examine the catalog of molecular clouds constructed from the GRS (Roman-Duval et al. 2010). If the AzTEC source is within the projected area of the cloud and its dense gas velocity is within 5 km s^{-1} of the cloud's ^{13}CO -defined velocity, then the distance to the AzTEC source is assigned to the cloud's distance. The distance, D, asymmetric distance uncertainties, $-\sigma(D)$, $+\sigma(D)$, resolution of the near-far side distance ambiguity, (near, far, uncertain), and distance reference for each linked AzTEC source are listed in Table 2.

The distributions of V_{LSR} values derived from the dense gas spectra (dark histogram) and ^{13}CO spectra (light grey histogram) are shown in Figure 4 (left). The distributions are similar with peaks at 50 km s^{-1} , 80 km s^{-1} and 110 km s^{-1} that correspond to the expected velocities of the far Sagit-

Table 3. AzTEC ^{13}CO Velocities and Dust Column Densities. The full table is available in the electronic version of the paper

AzTEC ID	$V(^{13}\text{CO})$ (km s^{-1})	C_v	N_{H} (10^{22} cm^{-2})	$-\sigma(N_{\text{H}})$ (10^{22} cm^{-2})	$+\sigma(N_{\text{H}})$ (10^{22} cm^{-2})
1	100.4	1.2	2.05	0.99	0.82
2	98.1	1.2	2.00	0.97	0.79
3	102.1	2.5	1.85	0.93	0.78
4	104.1	14.8	1.93	0.92	0.76
5	102.2	1.8	2.08	0.99	0.83
6	98.3	2.0	2.11	1.01	0.83
7	104.0	6.3	1.98	0.98	0.76
8	50.5	1.1	2.24	1.07	0.90
9	98.1	2.2	2.13	1.01	0.82
10	100.4	1.9	1.88	0.95	0.79

tarius arm, the near Scutum arm and the far Scutum arm respectively (Steiman-Cameron et al. 2010; Koda et al. 2016). Figure 4 also shows the distribution of distances to AzTEC sources directly or indirectly linked to BGPS objects or linked to GRS ^{13}CO clouds. Most of these sources are located on the near side of the terminal velocity distance of 7.6 kpc at $l=24.5$ assuming the rotation curve of Reid et al. (2009). However there are several clusters of sources at distances 9.25, 10, and 11.5 kpc located on the far side of the Galaxy.

3.4 Column density, mass, and mean volume density

The derived properties of mass, mean volume density, and column density are useful measures to classify millimeter sources of dust continuum emission into clouds, clumps, and cores (Dunham et al. 2011). There are obvious dependencies on distance for mass (D^2) and volume density (D^{-1}) but these trends are also a product of the effective spatial filtering as part of the removal of the atmospheric contribution to the signal that depends on the angular scale of the cloud or clump (Battisti & Heyer 2014). For the BGPS sample, the effect is to generally identify more nearby objects as cores, sources at intermediate distances as clumps, and more distant objects as clouds (Dunham et al. 2011; Ellsworth-Bowers et al. 2015b).

To gain a better understanding of the nature of the identified AzTEC compact sources, we calculate the hydrogen column density for all detected objects and molecular hydrogen mass and mean volume density for the subset of objects with a defined distance. The dust emission at $\lambda 1.1$ mm is assumed to be optically thin, which allows a simple relationship between hydrogen column density, N_{H} , and measured surface brightness, $S_{\text{peak}}/\Omega_{\text{A}}$,

$$N_{\text{H}} = \left(\frac{S_{\text{peak}}}{\Omega_{\text{A}}} \right) \frac{R}{\mu m_{\text{H}} \kappa_{1.1\text{mm}} B_{\nu}(T_{\text{D}})} \quad (4)$$

where Ω_{A} is the solid angle of the AzTEC beam, R is the gas to dust mass ratio, $\mu=2.4$ is the mean atomic weight, and m_{H} is the mass of the hydrogen atom. $\kappa_{1.1\text{mm}}$ is dust opacity at $\lambda 1.1$ mm and $B_{\nu}(T_{\text{D}})$ is the Planck function evaluated at $\lambda 1.1$ mm and a single temperature, T_{D} for the dust grains. We adopt the conventional values for the constants: $R=100$, $\kappa_{1.1\text{mm}}=1.14 \text{ cm}^2 \text{ g}^{-1}$ (Ossenkopf & Henning 1994). Without

an infrared-mm spectral energy distribution, a dust temperature for each source can not be derived. Rather, for each source, a gaussian distribution of dust temperatures centered on 16 K with a dispersion of 4 K is assumed that is based on recent Herschel estimates of dust temperatures for a set of infrared dark clouds (IRDCs) (Traficante et al. 2015) and the median gas kinetic temperature (Svoboda et al. 2016). From this distribution, a Monte-Carlo calculation is executed that randomly samples the dust temperature distribution as input to equation 4 while also considering photometric errors. For 1024 realizations, the result is a distribution of N_{H} values. The mean value of this distribution is assigned to the column density of the source. Both lower and upper $1-\sigma$ errors are derived from the shape of the N_{H} distribution. These errors are primarily due to the sampling of the temperature distribution. The column density and uncertainties are listed in Table 3 for all AzTEC sources.

This column density represents an average value over the solid angle of the telescope beam. As these objects are identified as point sources or are marginally resolved, the solid angle of one or more sources within the beam is smaller than Ω_{A} such that actual source column densities would be larger by the factor equal to the reciprocal of the beam filling factor of sources. Also, our assumed dust temperature distribution may not apply to all objects – especially those with embedded, compact HII regions excited by massive stars that can locally heat the dust to temperatures in excess of 16 K (Merello et al. 2015). The adoption of a higher dust temperature leads to smaller column densities.

We acknowledge that free-free radiation from an associated compact HII region may contribute to the observed $\lambda 1.1$ mm emission. Schloerb et al. (1987) found contributions of free-free emission to the $\lambda 1.3$ mm band to be less than 10% in Orion, 25% in W49A, and dominant in W51 IRS2. More recently, Zhang et al. (2014) estimate that 25-55% of the emission at $\lambda 1.3$ mm is free-free radiation from the hypercompact HII region G35.58-0.03. As discussed in §3.5, only 14 of the AzTEC sources are associated with a compact HII region so contamination of the dust emission by free-free emission is likely to be limited to a small number of sources. For 11 of these sources, we extrapolate the available 5 GHz flux (Purcell et al. 2013) to 273 GHz assuming a spectral index of -0.1. For those sources whose measured angular extent at 5 GHz is greater than $8.5''$, we also apply a correction to account for the flux that would be collected within the AzTEC solid angle. The estimated

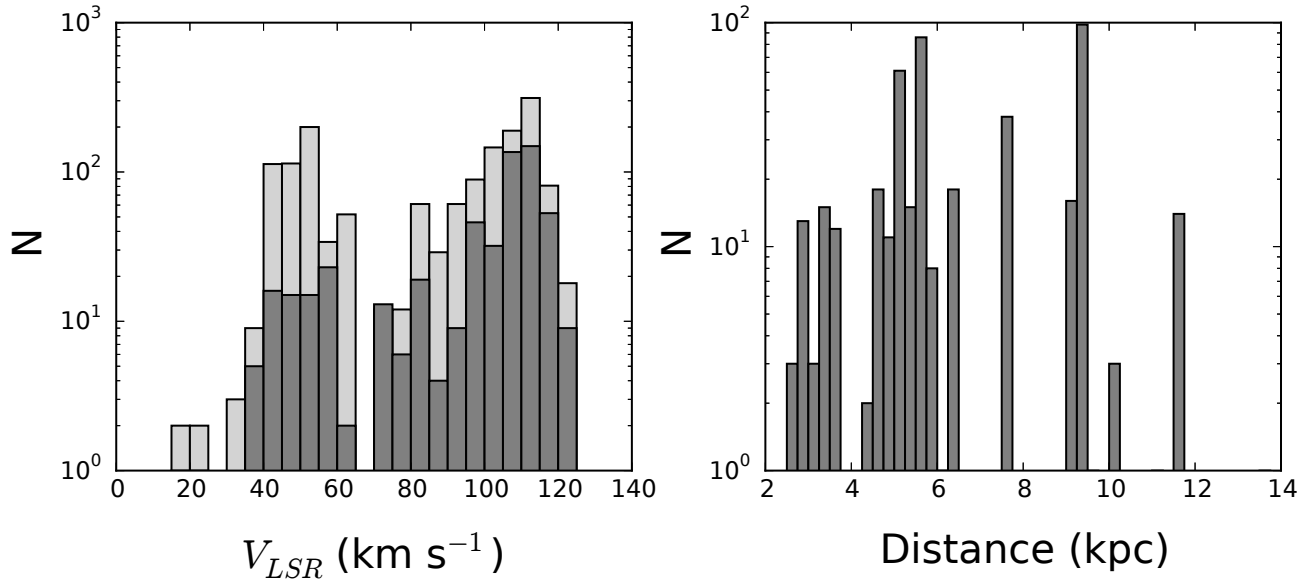


Figure 4. (left) Distribution of V_{LSR} values derived from high density gas tracer (dark histogram) and ^{13}CO J=1-0 emission (light histogram). (right) The distribution of distances to the subset of AzTEC sources linked to BGPS objects with defined distances from [Ellsworth-Bowers et al. \(2015a\)](#) and [Svoboda et al. \(2016\)](#) or linked to ^{13}CO clouds catalogued by [Roman-Duval et al. \(2010\)](#).

fractional contribution of free-free emission is the ratio of this extrapolated flux to that measured by AzTEC. Four of the 11 sources have fractional contributions greater than 50% and seven of the sources have contributions in excess of 20%. In these cases, the dust derived column densities, uncorrected for free-free contamination, are upper limits.

The distribution of hydrogen column density for all AzTEC defined sources is shown in Figure 5. The sharp cutoff for column densities less than $1.3 \times 10^{22} \text{ cm}^{-2}$ arises from the $>3\sigma$ requirement for source inclusion, the adopted constant for source solid angle, Ω_A , and the uniform sensitivity of the map from which sources are identified. The median value of this distribution is $1.7 \times 10^{22} \text{ cm}^{-2}$, which is a factor of 4 larger than the weighted BGPS column density integrated over the source area for starless and protostellar BGPS sources derived by [Svoboda et al. \(2016\)](#) and 2 times larger than their mean-weighted peak column density. The higher angular resolution of AzTEC and the compact definition of the extracted sources lead to the detection of objects with systematically higher column densities than typical BGPS sources.

The mass of material within the AzTEC beam including contributions from helium is

$$M = \mu m_{\text{H}} D^2 N_{\text{H}} \Omega_A \quad (5)$$

where D is the distance to the source. The distribution of derived source masses is shown in Figure 5 (middle). The masses range from 3.4 to $1625 M_{\odot}$ and correspond to low mass dense cores that may form a single low-mass star to massive clumps from which several massive stars and small stellar clusters could develop. Assuming a dust temperature of 16 K, our sensitivity limits can recover masses of compact sources greater than $10 M_{\odot} (D/4 \text{ kpc})^2$ with signal to noise of 4.

The mean volume density of each AzTEC source with

a defined distance is estimated from the column density and projected physical size, which is assumed to be equal to the line of sight depth,

$$n = \frac{N_{\text{H}}}{\theta D} \quad (6)$$

where θ is the AzTEC half-power beam width in radians. The densities are typical of resolved, dense cores found in nearby star forming regions. Moreover, these are generally higher than mean volume densities derived for BGPS sources ([Dunham et al. 2011](#); [Battisti & Heyer 2014](#); [Svoboda et al. 2016](#)).

Masses and mean volume densities and corresponding 1σ uncertainties are compiled in Table 4. In summary, AzTEC sources have lower masses, higher column and volume densities than BGPS sources and correspond to localized, high density peaks embedded within a lower density substrate of gas.

3.5 Linking AzTEC sources to compact HII regions and Methanol Masers

We seek to connect the compact, high density regions detected by AzTEC with signatures of massive star formation. Such signatures include UCHII regions and Class II methanol masers that trace an even earlier stage of forming a massive star.

For the compact HII regions, the source catalogs from the Coordinated Radio and Infrared Survey for High-mass star formation (CORNISH) at a frequency of 5 GHz ([Purcell et al. 2013](#)) and the HI, OH, Recombination Line Survey of the Milky Way (THOR) at a frequency of 1.4 GHz ([Bihl et al. 2016](#)) are examined for proximity to a given AzTEC source in the field. To isolate sources of free-free emission in the THOR wavelength band of 1.4 GHz, we

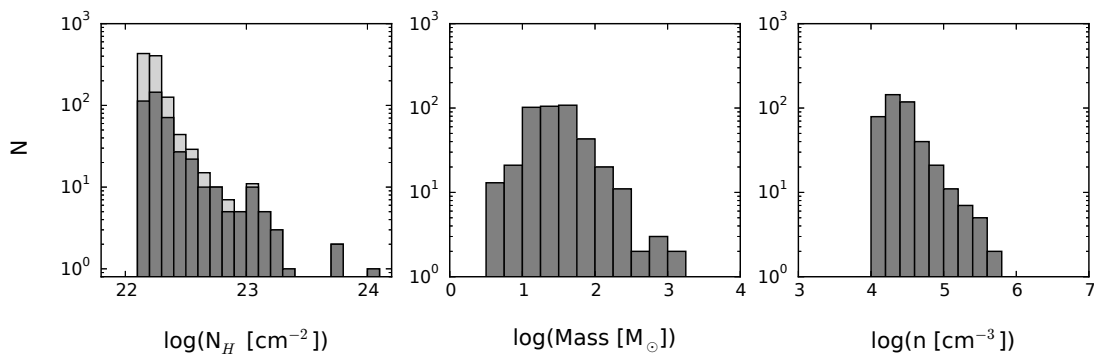


Figure 5. (left) Distribution of the logarithm of hydrogen column density for $P_J < 0.2$ sources in the field (light grey) and those with defined distances (dark grey). (middle) Distribution of the logarithm of gas mass within AzTEC sources. (right) Distribution of the logarithm of mean volume gas density of AzTEC sources.

Table 4. AzTEC Masses and Mean Volume Densities. The full table is available in the electronic version of the paper

AzTEC ID	M (M_\odot)	$-\sigma(M)$ (M_\odot)	$+\sigma(M)$ (M_\odot)	n (cm^{-3})	$-\sigma(n)$ (cm^{-3})	$+\sigma(n)$ (cm^{-3})
22	134.2	54.2	44.6	31500.0	12700.0	10400.0
26	107.3	44.6	34.0	25200.0	10400.0	7940.0
27	13.8	6.9	6.3	25600.0	12600.0	11300.0
29	67.9	31.3	25.3	16000.0	7340.0	5930.0
34	13.6	6.6	5.8	25200.0	12000.0	10500.0
39	18.9	8.7	7.3	33200.0	15000.0	12500.0
42	23.6	10.4	8.8	39200.0	17100.0	14400.0
44	24.2	10.1	9.5	42600.0	17500.0	16400.0
46	17.2	8.2	7.2	28500.0	13400.0	11800.0
48	14.0	6.8	5.4	23300.0	11100.0	8810.0

only consider sources with spectral indices > 0.1 derived from the sub-bands of the THOR data. A link between an AzTEC source and a catalogued HII region is established if the distance between the radio continuum centroid coordinates and the AzTEC peak coordinates is less than $10''$. The 14 AzTEC sources linked to HII regions from these catalogs are compiled in Table 5.

A Class II methanol maser from the catalog compiled by Breen et al. (2015) is linked to the AzTEC source if its position is within $10''$ of the AzTEC source position. Table 6 lists the 14 AzTEC sources that are positionally linked to the methanol masers. Figure 2 shows examples of AzTEC sources associated with these signatures of massive star formation.

4 FRAGMENTATION OF MASSIVE CLUMPS

The BGPS source catalog provides a Galactic census of massive clumps that are responsible for clustered star formation in molecular clouds. In most cases, the size, mass, and column density of the BGPS sources are similar to large fragments or clumps embedded within larger molecular clouds and are often coincident with infrared dark clouds (Peretto et al. 2016). Such objects may form small stellar clusters so one might expect that these are further fragmented into smaller, less massive but higher density objects that act as seeds for newborn stars. The resolution and sensitivity of the LMT data enable an examination of the frag-

mentation of the dense, massive clumps and filaments in molecular clouds distributed over a large range of Galactic radii.

We define the AzTEC multiplicity as the number of AzTEC sources with P_J values less than 0.2 within a BGPS source boundary. Figure 6 shows the distribution of this multiplicity. While a single, embedded AzTEC source is the most frequent configuration, most BGPS objects contain two or more compact sources. In some cases, a BGPS source is highly fragmented with greater than 10 AzTEC objects within its domain. Possible processes responsible for this clump fragmentation include ambipolar diffusion (Lizano & Shu 1989), turbulent fragmentation (Padoan & Nordlund 2002), and gravitational Jeans' instability (Jappsen et al. 2005).

While our data can not address the role of magnetic fields and turbulence in the fragmentation of clumps, we can evaluate the expected outcome of Jeans' fragmentation in which the mass of the resultant sub-fragments are comparable to the Jeans' mass of the larger volume. The Jeans' mass of a BGPS object is

$$M_{J,BGPS} = \frac{\pi^{5/2}}{6} G^{-3/2} \rho^{-1/2} c_s^3 \quad (7)$$

where $c_s = (kT/\mu m_H)^{1/2}$ is the sound speed for isothermal gas, ρ is the mean density, and spherical geometry is assumed. Mean density and temperature values are taken from the compilation by Svoboda et al. (2016). The mean mass, $\langle m_{AzTEC} \rangle$, of all embedded AzTEC sources within

Table 5. AzTEC Sources Linked HII regions.

AzTEC ID	CORNISH Name	THOR Name	THOR Spectral Index
68	G024.4698+00.4954	null	-999.00
77	G024.4736+00.4950	null	-999.00
79	G024.4721+00.4877	G24.471+0.488	0.15
117	null	G24.677+0.549	1.19
150	G023.9564+00.1493	G23.956+0.150	0.61
263	null	G24.200+0.192	0.13
391	G024.1839+00.1199	null	-999.00
573	null	G23.988-0.089	-0.02
923	G024.4921-00.0386	G24.493-0.038	0.24
965	G024.7984+00.0967	G24.798+0.096	0.11
988	G024.7889+00.0824	null	-999.00
1038	G024.8497+00.0881	null	-999.00
1103	G024.9237+00.0777	null	-999.00
1219	G024.5065-00.2224	G24.507-0.223	0.20

Table 6. AzTEC Sources Linked Class II Methanol Masers.

AzTEC ID	Maser Name	l(Maser) (deg.)	b(Maser) (deg.)	V(Maser) (km s ⁻¹)
380	G24.541+0.312	24.5411	0.3121	106.5
470	G24.329+0.144	24.3287	0.1444	110.3
494	G24.461+0.198	24.4612	0.1980	125.5
573	G23.986-0.089	23.9861	-0.0890	65.1
585	G24.148-0.009	24.1479	-0.0091	17.4
599	G23.966-0.109	23.9661	-0.1092	70.9
611	G23.996-0.100	23.9964	-0.0995	68.2
923	G24.493-0.039	24.4934	-0.0389	115.2
988	G24.790+0.083a	24.7897	0.0832	113.3
1038	G24.850+0.087	24.8502	0.0874	110.0
1087	G24.920+0.088	24.9196	0.0882	53.3
1121	G24.943+0.074	24.9428	0.0741	46.6
1237	G24.676-0.150	24.6755	-0.1499	116.1
1409	G24.634-0.324	24.6340	-0.3237	35.6

a BGPS object is calculated. We also compute the Mach number of non-thermal motions from the measured NH₃ velocity dispersion, $\sigma_{v,NT}/c_s = (\sigma_{v,NH_3}^2 - c(NH_3)^2)^{1/2}/c_s$, where $c(NH_3) = (kT/17m_H)^{1/2}$ is the thermal speed of ammonia molecules. Here, we assume the NH₃ velocity dispersion from the peak dust position is representative of the velocity dispersion over the full clump. Values of the Mach number for this subset of BGPS objects range from 1.6-7.2. We caution that the Jeans' criterion for fragmentation, which is based on thermal pressure support against self-gravity, may not apply to the regime where the gas motions are strongly supersonic.

Figure 7 shows the variation of the ratio $\langle m_{AzTEC} \rangle / M_{J,BGPS}$ as a function of the BGPS mass, m_{BGPS} , derived from the dust emission (Svoboda et al. 2016). The colors and sizes of the points represent the Mach number and distance respectively. The results of this analysis are mixed. Most of the Galactic near-side ($D < 6$ kpc), moderate Mach number BGPS objects harbor AzTEC fragments with masses comparable to the BGPS Jeans' mass as expected for Jeans' fragmentation. Yet, there are also several strongly supersonic BGPS objects with $\langle m_{AzTEC} \rangle \approx M_{J,BGPS}$. Some of these objects are associated with infrared dark clouds (Peretto & Fuller 2009) while others are coincident with HII regions that may increase the NH₃ velocity dispersion at the

peak dust position. All of the Galactic far-side ($D > 9$ kpc) BGPS objects in this subsample have $\langle m_{AzTEC} \rangle / M_{J,BGPS}$ greater than 3. This supercritical Jeans' mass state likely arises from the inability of our observations to resolve the BGPS Jeans' length in these more distant objects. In this case, the beam is integrating over multiple Jeans' lengths leading to masses in excess of the clump Jeans' mass. For a gas temperature of 16 K and a volume density of 1666 cm⁻³ corresponding to the weighted average of starless and protostellar clumps (Svoboda et al. 2016), a typical BGPS Jeans' length is 0.23 pc. This scale is not resolved by the 8.5'' LMT/AzTEC beam at distances greater than 5.5 kpc.

4.1 The fraction of dense gas in BGPS clumps

The correlation of star formation rate with the amount of dense gas has been established on the scales of the central regions of galaxies (Gao & Solomon 2004), massive clumps of molecular clouds (Wu et al. 2005), and local star forming regions (Heiderman et al. 2010; Lada et al. 2012; Gutermuth et al. 2011). In these cases, dense gas refers to regions with high visual extinction or molecular line emission that requires high excitation conditions. Such lines include

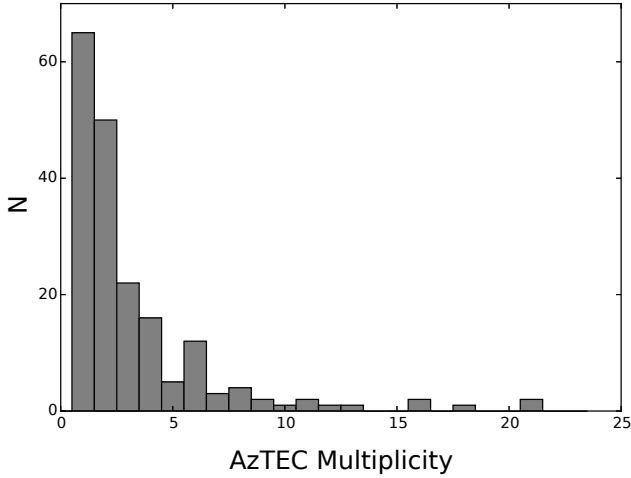


Figure 6. Distribution of AzTEC multiplicity in BGPS objects.

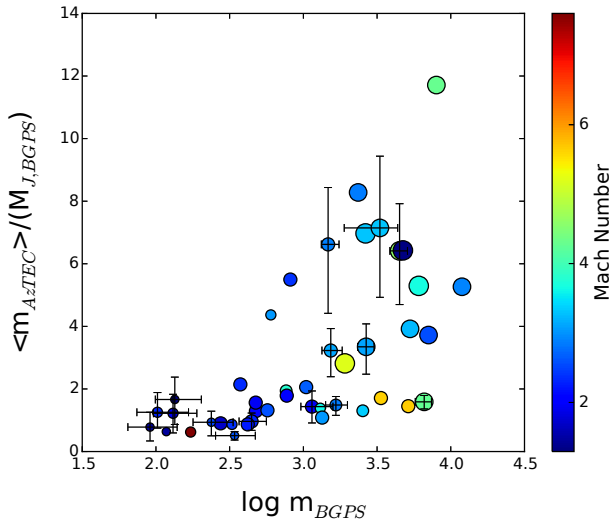


Figure 7. The ratio of the mean mass of AzTEC sources to the BGPS Jeans' mass as a function of BGPS mass derived from dust emission. The color of the points denote the Mach number for an isothermal equation of state. The color table ranges between the minimum Mach number of 1.6 to the maximum of 7.2. The size of the points are proportional to the distance over the range 3.3 kpc to 13 kpc. For BGPS sources with distances less than 6 kpc, the AzTEC source masses are comparable to the Jeans' mass of the overlying clump. More distant sources exhibit larger values of $\langle m_{AzTEC} \rangle / M_{J,BGPS}$.

the rotational transitions of HCN, N_2H^+ , HCO^+ , and CS with critical densities of $\sim 10^4 \text{ cm}^{-3}$ or higher.

To better understand this correlation between star formation rate and the mass of available dense gas, a key measure to evaluate is the fraction of a clump's mass that is distributed into subfragments at higher density as these provide the local reservoir of gas that fuels the current or impending formation of stars. Assuming the same dust temperature for

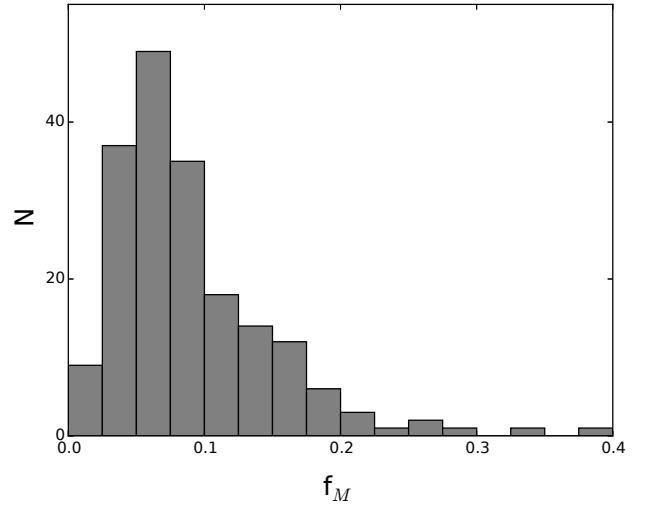


Figure 8. Distribution of the fraction of 11.1 mm flux contributed by embedded AzTEC sources to the total flux measured by the BGPS. Assuming the same dust temperature between the BGPS and AzTEC sources, this ratio corresponds to the fractional mass of the clump distributed into small, dense fragments.

the BGPS object and its linked AzTEC sources, this fractional mass, f_M , is directly calculated from the ratio of total flux from all AzTEC sources to the flux measured by the BGPS,

$$f_M = \frac{\sum M_{i,AzTEC}}{M_{BGPS}} = \frac{\sum S_{i,AzTEC}}{S_{BGPS}} \quad (8)$$

where the sum is over all AzTEC sources within the BGPS source. Figure 8 shows the distribution of f_M for all BGPS sources linked to 1 or more AzTEC sources. The median value is 0.075 with the standard deviation of 0.059 and a mean, 1σ measurement uncertainty of 0.026. This fraction does not include isolated, low mass regions that are external to the compiled AzTEC sources but whose dust emission level falls below our sensitivity limit. The contribution of low mass fragments or cores to the total clump mass is included in the BGPS integrated flux measure. Therefore, this calculation of the dense gas fraction could be affected by incompleteness of AzTEC to detect low mass objects. However, we find no decreasing trend in f_M values with increasing distance as one would expect as low-mass sources fall below our mass sensitivity limit. The absence of such a trend suggests that most low mass, compact sources are primarily contained within the solid angle of the extracted AzTEC sources so that their contributions are included and our calculation of the fractional mass of dense gas is not severely underestimated.

Given the mass distribution of AzTEC sources, these are not representative of protostellar cores that may collapse into single stars. Rather, the AzTEC sources are likely further structured into even denser gas subfragments as shown by sub-arcsecond interferometry of star forming regions over fields comparable to the AzTEC beam solid angle (Beuther et al. 2007; Brogan et al. 2016; Cyganowski et al.

2017). Thus, the fraction of the clump mass distributed into denser, protostellar cores is likely much smaller than 8%.

The BGPS clumps reside within the larger structures of molecular clouds that are typically probed by CO and its isotopologues (Heyer & Dame 2015). From a sample of over 300 clouds, Battisti & Heyer (2014) determined the fractional mass of a cloud distributed into BGPS sources is $f_B=11\%$ with a population dispersion of 6%. For nearby star forming regions, Lada et al. (2012) derived a similar fractional mass for regions with $A_V > 8$ magnitudes. Taking this value for the fractional mass of BGPS sources in molecular clouds within our survey field, then AzTEC sources comprise 0.008 ± 0.008 of a cloud mass. Protostellar cores within the AzTEC source constitute an even smaller fraction. These results emphasize that within time intervals smaller than the dynamical time of AzTEC sources, only a small fraction of a molecular cloud is configured for the production of new stars.

5 HIGH MASS STAR FORMATION THRESHOLDS

The formation of a high mass ($m_* > 8 M_\odot$) star within the ISM is a rare event, which implies that restrictive conditions are required. For the core accretion description of high mass star formation, the protostellar core must have sufficient initial mass to produce a massive star and a sufficient accretion rate to overcome radiation pressure (McKee & Tan 2003). In addition, fragmentation of the core must be suppressed to allow for most of the mass to accrete onto a singular, developing star. Radiative heating from recently formed low mass stars can increase the Jeans' mass of the local core and suppress any further fragmentation. Krumholz & McKee (2008) derive a mass surface density threshold, Σ_{cr} , at which the light-to-mass ratio of accreting, low mass protostars is equal to light-to-mass ratio necessary to suppress fragmentation. For solar metallicity and a background dust temperature of 10 K, Σ_{cr} varies between 0.7 and 1 g cm^{-2} for stellar masses between 10 and $100 M_\odot$. An empirically defined mass threshold of clumps was identified by Kauffmann & Pillai (2010) for a set of infrared dark clouds with radius r , $m_{cl,min}=870 M_\odot(r/\text{pc})^{1.33}$ that separates IRDCs with and without signatures of massive star formation. This minimum mass corresponds to a mass surface density threshold of $0.05 \text{ g cm}^{-2} (r/1 \text{ pc})^{-0.67}$. Urquhart et al. (2014) identified a similar mass surface density threshold based on a sample of ATLASGAL clumps linked to various tracers of high mass star formation.

To further investigate this proposed mass surface density threshold, we examine our sample of AzTEC sources. Figure 9 shows the location of the identified AzTEC objects within the mass- Σ plane that is frequently used to distinguish the environments of low and high mass star formation (Tan et al. 2014). Sources are differentiated by their association with UCHII regions (red points), Class II methanol masers (green points), or absence of either of these signatures (blue points). Several AzTEC sources harbor both a compact HII region and a Class II methanol maser. The large sample of BGPS sources analyzed by Svoboda et al. (2016) with derived masses are represented as a 2-dimensional histogram. The diagonal lines show loci of constant radius in parsecs. The mass surface density thresholds to massive star formation proposed by Krumholz & McKee (2008) and

Kauffmann & Pillai (2010) are shown as the grey wedge and solid black line respectively. We re-emphasize that the derived AzTEC mass surface densities and source sizes are lower and upper limits respectively since these sources are marginally resolved or unresolved. The apparent correlation between mass and mass surface density of the AzTEC points or equivalently, equal source size, is a result of adopting a common solid angle, Ω_A , for each source. The parallel bands of points correspond to distinct clusters of AzTEC sources located at different distances (see Figure 4).

Most of the AzTEC sources associated with ultra-compact HII regions are located above the KP2010 threshold that affirms this empirically derived limit. More interestingly, 10 of the 13 AzTEC sources linked to Class II methanol masers are positioned at or above the more constraining KM08 threshold within the measurement errors. This strong bias offers provisional evidence for high mass star forming regions satisfying the restrictive conditions that suppress core fragmentation. To more fully evaluate these conditions, higher angular resolution measurements are required that can discern whether one or more objects are present within these AzTEC sources. A single, massive fragment identified within an AzTEC source with these mass surface density values or higher would provide powerful evidence for the suppression of fragmentation that leads to the formation of a massive star.

6 CONCLUSIONS

Sensitive, imaging observations with $8.5''$ angular resolution of the 1.1mm dust continuum emission along the Galactic plane have been used to examine the properties of high density fragments and subfragments within molecular clouds. The identified objects are embedded within larger clumps of molecular clouds as measured by the Bolocam Galactic Plane Survey. The AzTEC sources have larger column and mean volume densities and smaller masses than the overlying clumps but may also be further fragmented when observed with higher angular resolution. The AzTEC sources comprise on average, 8% of the mass of the BGPS clump in which these reside and 0.8% of the mass of the parent molecular cloud. The embedded AzTEC sources have masses that are a factor of 1-10 times larger than the Jeans' mass of the BGPS object. The mass surface densities of AzTEC sources linked to ultra-compact HII regions are typically greater than the mass surface density implied by the empirical mass-size threshold (Kauffmann & Pillai 2010). For AzTEC sources associated with Class II methanol masers that mark an earlier phase of massive star formation, the mass surface densities exceed 0.7 g cm^{-2} that approaches the critical threshold proposed by Krumholz & McKee (2008).

ACKNOWLEDGMENTS

We appreciate the useful comments provided by referee that improved the clarity of this manuscript. This research made use of Astropy, a community-developed core Python package for Astronomy (Astropy Collaboration, 2013). We also acknowledge the long-term financial support from the Mexican Science and Technology Funding Agency, Consejo Nacional

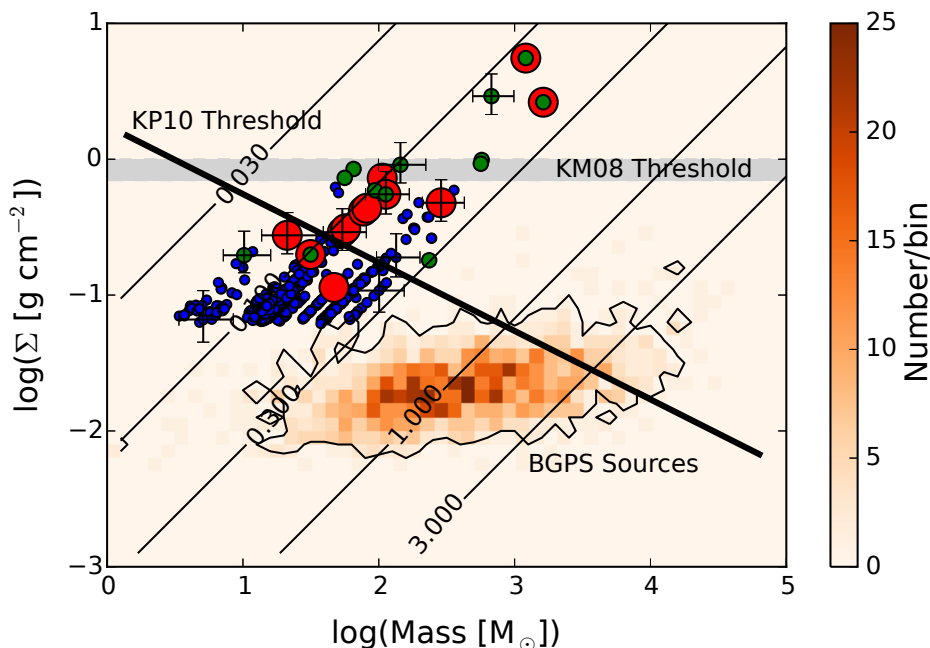


Figure 9. Distribution of AzTEC sources in the mass- Σ plane linked to UCHII regions (red), methanol masers (green), and no signatures to massive star formation (blue). Since the AzTEC sources are unresolved or marginally resolved, the Σ values are lower limits to structures within the AzTEC 8.5'' beam. The half-tone is a 2D histogram of mass and Σ values for 1640 BGPS sources compiled by Svoboda et al. (2016) with established masses. The horizontal grey wedge marks the mass surface density threshold proposed by Krumholz & McKee (2008) and the solid back line represents the empirical threshold of Kauffmann & Pillai (2010). For clarity, every 10th errorbar is plotted. Labeled diagonal lines are loci of constant radius in parsecs, $r=(\text{Mass}/\pi\Sigma)^{1/2}$.

de Ciencia y Tecnología (CONACYT), during the construction and early science phase of the Large Millimetre Telescope Alfonso Serrano, as well as support from the US National Science Foundation via the University Radio Observatory program, the Instituto Nacional de Astrofísica, Óptica y Electrónica (INAOE), and the University of Massachusetts (UMASS).

REFERENCES

- André P., Di Francesco J., Ward-Thompson D., Inutsuka S.-I., Pudritz R. E., Pineda J. E., 2014, *Protostars and Planets VI*, pp 27–51
- Battisti A. J., Heyer M. H., 2014, *ApJ*, **780**, 173
- Beuther H., Leurini S., Schilke P., Wyrowski F., Menten K. M., Zhang Q., 2007, *A&A*, **466**, 1065
- Bühr S., et al., 2016, *A&A*, **588**, A97
- Breen S. L., et al., 2015, *MNRAS*, **450**, 4109
- Brogan C. L., Hunter T. R., Cyganowski C. J., Chandler C. J., Friesen R., Indebetouw R., 2016, *ApJ*, **832**, 187
- Cyganowski C. J., Brogan C. L., Hunter T. R., Smith R., Kruijssen J. M. D., Bonnell I. A., Zhang Q., 2017, *MNRAS*, **468**, 3694
- Dunham M. K., Rosolowsky E., Evans II N. J., Cyganowski C., Urquhart J. S., 2011, *ApJ*, **741**, 110
- Ellsworth-Bowers T. P., Rosolowsky E., Glenn J., Ginsburg A., Evans II N. J., Battersby C., Shirley Y. L., Svoboda B., 2015a, *ApJ*, **799**, 29
- Ellsworth-Bowers T. P., et al., 2015b, *ApJ*, **805**, 157
- Gao Y., Solomon P. M., 2004, *ApJ*, **606**, 271
- Ginsburg A., et al., 2013, *ApJS*, **208**, 14
- Gutermuth R. A., Pipher J. L., Megeath S. T., Myers P. C., Allen L. E., Allen T. S., 2011, *ApJ*, **739**, 84
- Heiderman A., Evans II N. J., Allen L. E., Huard T., Heyer M., 2010, *ApJ*, **723**, 1019
- Heyer M., Dame T. M., 2015, *ARA&A*, **53**, 583
- Jackson J. M., et al., 2006, *ApJS*, **163**, 145
- Jappsen A.-K., Klessen R. S., Larson R. B., Li Y., Mac Low M.-M., 2005, *A&A*, **435**, 611
- Kauffmann J., Pillai T., 2010, *ApJ*, **723**, L7
- Koda J., Scoville N., Heyer M., 2016, *ApJ*, **823**, 76
- Krumholz M. R., McKee C. F., 2008, *Nature*, **451**, 1082
- Krumholz M. R., Tan J. C., 2007, *ApJ*, **654**, 304
- Lada C. J., Forbrich J., Lombardi M., Alves J. F., 2012, *ApJ*, **745**, 190
- Lizano S., Shu F. H., 1989, *ApJ*, **342**, 834
- McKee C. F., Tan J. C., 2003, *ApJ*, **585**, 850
- Menten K. M., 1991, *ApJ*, **380**, L75
- Merello M., Evans II N. J., Shirley Y. L., Rosolowsky E., Ginsburg A., Bally J., Battersby C., Dunham M. M., 2015, *ApJS*, **218**, 1
- Molinari S., et al., 2016, *A&A*, **591**, A149
- Ossenkopf V., Henning T., 1994, *A&A*, **291**, 943
- Padoan P., Nordlund Å., 2002, *ApJ*, **576**, 870
- Perera T. A., Wilson G. W., Scott K. S., Austermann J. E., Schaar J. R., Mancera A., 2013, *PASP*, **125**, 838
- Peretto N., Fuller G. A., 2009, *A&A*, **505**, 405
- Peretto N., Lenfestey C., Fuller G. A., Traficante A., Molinari S., Thompson M. A., Ward-Thompson D., 2016, *A&A*, **590**, A72
- Purcell C. R., et al., 2013, *ApJS*, **205**, 1
- Reid M. J., et al., 2009, *ApJ*, **700**, 137
- Roman-Duval J., Jackson J. M., Heyer M., Rathborne J., Simon R., 2010, *ApJ*, **723**, 492
- Schlingman W. M., et al., 2011, *ApJS*, **195**, 14
- Schloerb F. P., Snell R. L., Schwartz P. R., 1987, *ApJ*, **319**, 426

- Schuller F., et al., 2009, *A&A*, **504**, 415
Scott K. S., et al., 2008, *MNRAS*, **385**, 2225
Shirley Y. L., et al., 2013, *ApJS*, **209**, 2
Steiman-Cameron T. Y., Wolfire M., Hollenbach D., 2010, *ApJ*, **722**, 1460
Svoboda B. E., et al., 2016, *ApJ*, **822**, 59
Tan J. C., Beltrán M. T., Caselli P., Fontani F., Fuente A., Krumholz M. R., McKee C. F., Stolte A., 2014, *Protostars and Planets VI*, pp 149–172
Traficante A., Fuller G. A., Peretto N., Pineda J. E., Molinari S., 2015, *MNRAS*, **451**, 3089
Urquhart J. S., et al., 2014, *MNRAS*, **443**, 1555
Wilson G. W., et al., 2008, *MNRAS*, **386**, 807
Wu J., Evans II N. J., Gao Y., Solomon P. M., Shirley Y. L., Vanden Bout P. A., 2005, *ApJ*, **635**, L173
Zhang C.-P., Wang J.-J., Xu J.-L., Wyrowski F., Menten K. M., 2014, *ApJ*, **784**, 107